# Bismuth and antimony halometalates containing photoswitchable ruthenium nitrosyl complexes

Artem Mikhailov, Nikita Korobeynikov, Andrey Usoltsev, Sergey Adonin, Gennadiy Kostin, Dominik Schaniel

# Bismuth and antimony halometalates containing photoswitchable ruthenium nitrosyl complex

Artem Mikhailov[a], Nikita Korobeynikov[b], Andrey Usoltsev[b], Sergey A. Adonin[b], Gennadiy A. Kostin[b], Dominik Schaniel[a]

[a] Université de Lorraine, CNRS, CRM2, UMR 7036, Nancy 54000, France

[b] Nikolaev Institute of Inorganic Chemistry, Siberian Branch of the Russian Academy of Sciences, 3 Acad. Lavrentiev Avenue, Novosibirsk 630090, Russian Federation

## Abstract

The first examples of Bi(III) and Sb(III) halide compounds combined with a photoswitchable ruthenium nitrosyl unit are reported. The structures of $[RuNOPy_4Br]_4[Sb_2Br_8][Sb_3Br_{12}]_2$ (**1**) and $(H_3O)[RuNOPy_4Br]_4[Bi_2Br_9]_3{\cdot}3H_2O$ (**2**) were determined by X-ray diffraction, and exhibit three different structural types of Group 15 halometalates. Low-temperature IR-spectroscopy measurements reveal that irradiation of **1** at 365 nm switches a stable Ru-NO (GS) unit to a metastable Ru-ON (MS1) linkage. Moreover, the light excitation of **2** at 365 or 405 nm induces the additional formation of a side-bond isomer Ru-$\eta^2$-(NO) (MS2). The reverse reactions MS1/MS2→GS can be induced by red-infrared light irradiation or by heating at temperatures > 200 K. The obtained synthetic and spectroscopic data open the way for the preparation of hybrid halide complexes with a variety of photoswitchable complexes ($NO_2$, $SO_2$, $N_2$, etc.), as well as give an insight on the behavior of light induced species embedded into polynuclear halides.

## Introduction

There is an intensively ongoing search for novel hybrid materials for the creation of photovoltaic devices [1–3]. Among the prominent perovskite-like materials, there are antimony and bismuth halide complexes [4–8]. Compared to known Pb-based perovskites these lead-free halide compounds offer thus potentially interesting environment-friendly alternatives. Yet, the devices based thereupon show significantly lower power conversion efficiency than the Pb-based ones (≈ 4% vs up to 25% [6,9]), but this area is still developing so it can be expected that higher performances can be achieved.

Despite the outstanding photovoltaic performance of perovskite or perovskite-like compounds, there are obstacles that prevent their wide practical usage, such as moisture-sensitivity, decreased durability with respect to heat or light. One of the possible ways to ensure the sustainability of the photovoltaic device is the introduction of other molecules to the structure of the perovskite. For example, the combination of perovskite with porphyrin metal complexes can increase moisture and thermal stability of a solar cell [10,11], while the combination with an azobenzene photoswitch can increase the stability against UV light [12,13].

Other types of molecular photoswitches, such as those based on a metal nitrosyl compound might offer similar potentialities in the design of perovskite-like materials. It was shown for ruthenium nitrosyl complexes that a stable group Ru-NO (GS) can be triggered by light to the Ru-ON (MS1) and Ru-$\eta^2$-(NO) (MS2) linkages [14,15]. Moreover, by the wise choice of the excitation wavelength, the system can be switched between all these linkage isomers [16,17]. Another feature of MS1 and MS2 is their absorption properties. Usually both isomers have much higher absorption in UV and infrared range with respect to GS [18]. Thus, the application of nitrosyl photoisomerization is potentially interesting regarding the combination with perovskite-like compound for the modulated protection against incident light. However, up to date there are no known structures of ruthenium nitrosyl complexes combined with antimony or bismuth halide compounds. At least two fundamental questions arise immediately: i) is it possible to synthesize the compound containing in the structure both halide pnictogen and ruthenium nitrosyl building block; ii) given the desired compound is obtained, do photoswitching properties of Ru-NO group persist in the obtained hybrid compound?

In order to answer these questions, we report for the first time the synthesis of Bi and Sb halide complexes containing *trans*-$[RuNOPy_4Br]^{2+}$ cation. The photoswitching properties are investigated by infrared spectroscopy. The complex *trans*-$[RuNOPy_4Br]^{2+}$ is especially interesting since its photoswitchable properties were described recently in *trans*-$[RuNOPy_4Br](PF_6)_2$ salt [19,20], where high populations of MS1 and MS2 was observed (about 40 and 20%, respectively).

## Experimental

### Synthesis

Ruthenium complexes *trans*-$[RuNOPy_4OH](PF_6)_2$ and *trans*-$[RuNOPy_4F](ClO_4)_2$ were synthesized according to methods reported earlier [19,21].

$[RuNOPy_4Br]_4[Sb_2Br_8][Sb_3Br_{12}]_2$ (**1**)

66.3 mg (0.1 mmol) of *trans*-$[RuNOPy_4OH](PF_6)_2$ and 29.2 mg (0.1 mmol) of $Sb_2O_3$ were dissolved in 2 ml of concentrated HBr at 70°C. Then the reaction mixture was cooled to 5°C, and in one week the orange crystals of **1** were formed. Crystals were washed with $H_2O$ on a glass filter and dried with air. The yield is 60%. The powder XRD patterns of the bulk sample correspond to the theoretical patterns calculated from the crystal structure determined by single-crystal XRD (Fig. S1). Elemental analysis for $C_{80}H_{80}N_{20}O_4Br_{36}Sb_8Ru_4$ calculated/found, mass %: C 17.0/16.3, H 1.4/1.4, N 5.0/4.7

$(H_3O)[RuNOPy_4Br]_4[Bi_2Br_9]_3{\cdot}3H_2O$ (**2**)

66.3 mg (0.1 mmol) of *trans*-$[RuNOPy_4OH](PF_6)_2$ and 134 mg (0.3 mmol) of $BiBr_3$ were dissolved in 2 ml of concentrated HBr at 70°C. Then the reaction mixture was cooled to 5°C, and in one week the red-orange crystals of **2** were formed. Crystals were washed with $H_2O$ on a glass filter and dried with air. The yield is 60%. The method can be reproduced using *trans*-$[RuNOPy_4F](ClO_4)_2$ precursor instead of *trans*-$[RuNOPy_4OH](PF_6)_2$. The powder XRD patterns of the bulk sample correspond to the theoretical patterns calculated from the crystal structure determined by single-

crystal XRD (Fig. S2). Elemental analysis for $C_{80}H_{89}N_{20}O_8Br_{31}Bi_6Ru_4$ calculated/found mass %: C 17.2/17.9; H 1.6/2.3; N 5.0/4.7.

**Single-crystal X-Ray diffraction**

Single crystal X-ray diffraction data of complexes $[RuNOPy_4Br]_4[Sb_2Br_8][Sb_3Br_{12}]_2$ (**1**) and $(H_3O)[RuNOPy_4Br]_4[Bi_2Br_9]_3{\cdot}3H_2O$ (**2**) were collected on a Bruker Apex Duo diffractometer with CCDs using graphite-monochromated MoKα radiation (λ = 0.71073 Å) via 0.5° ω- and ϕ-scan techniques. Reduction of the experimental data was performed using the APEX2 suite. The structures were solved by SHELXT and refined by the full-matrix least-squares technique SHELXL [22] assisted with the Olex2 GUI [23]. The atomic displacement parameters of the ordered non-H atoms were refined using an anisotropic approximation. The hydrogen atoms of the pyridine ligands and water molecules were located geometrically and refined using the riding model with AFIX parameters 1.2 and 1.5, respectively. All water molecules were refined as neutral $H_2O$, $H_3O^+$ model was excluded due to the absence of evident residual peaks. Crystallographic characteristics, experimental data, and the structure refinements are listed in Table S1. The structures of $[RuNOPy_4Br]_4[Sb_2Br_8][Sb_3Br_{12}]_2$ (**1**) and $(H_3O)[RuNOPy_4Br]_4[Bi_2Br_9]_3{\cdot}3H_2O$ (**2**) have been deposited with the CCDC with deposition numbers 2202258 and 2202257, respectively.

**Hirshfeld surface analysis**

The Hirshfeld surfaces were calculated using Crystal Explorer [24,25]. This program allows the normalized contact distance $d_{norm}$ to be mapped onto the generated Hirshfeld surface. It is customary to map $d_{norm}$ using a red– white–blue scheme, where red denotes close intermolecular contacts (negative $d_{norm}$), blue denotes longer contacts (positive $d_{norm}$) and white denotes intermolecular contacts equal to the van der Waals radii of atoms in contact ($d_{norm}$ = 0). It is possible to obtain two-dimensional plots (fingerprint plots) from the surfaces mapped with $d_{norm}$ values. Derived from the Hirshfeld surface, these 2D-fingerprint plots provide a visual summary of the frequency of each combination of $d_e$ (radius of external atom) and $d_i$ (radius of internal atom) across the surface of a molecule, so they not only indicate which intermolecular interactions are present, but also the relative area of the surface corresponding to each kind of interaction. Points on the plot with no contribution on the surface are left uncoloured, and points with a contribution to the surface are coloured blue for a small contribution through green to red for points with the largest contribution.

**Spectroscopy**

IR-spectroscopy measurements with irradiation were performed using a Nicolet 5700 FT-IR spectrometer with a resolution of 2 $cm^{-1}$ in the range 400–4000 $cm^{-1}$. The sample (around 1-2 mg) was mixed with KBr (around 100 mg) and pressed into common pellets for IR measurements. The pellets were bonded onto the cold finger of a closed-cycle cryostat (Oxford Optistat) allowing to control the temperature in range 10 - 300 K. The irradiation procedures were performed by Thorlabs LEDs (Light Emitting Diodes) through KBr windows perpendicular to the samples with light of different wavelengths (365 – 1050 nm) with 50 - 200 mW optical power. To investigate the isothermal kinetics of MS1 and MS2 decay in $(H_3O)[RuNOPy_4Br]_4[Bi_2Br_9]_3{\cdot}3H_2O$ (**2**) the following protocol was applied: on the first stage the sample was irradiated at 100 K by 405 nm LED in order to generate a sufficient amount of MS1 and MS2 isomer; on the second stage the temperature was increased up to chosen value and then repeated measurement (the delay

between spectra was 60, 80 or 120 s) was performed in isothermal mode. Further, activation energy and frequency factors were determined in Arrhenius coordinates (Fig. 6). UV-vis spectra were recorded on a PG Instruments T60 UV-vis single-beam spectrophotometer.

## Results and discussion

### Structures of $[RuNOPy_4Br]_4[Sb_2Br_8][Sb_3Br_{12}]_2$ (1) and $(H_3O)[RuNOPy_4Br]_4[Bi_2Br_9]_3{\cdot}3H_2O$ (2)

Both **1** and **2** can be synthesized from *trans*-$[RuNOPy_4OH](PF_6)_2$ and corresponding pnictogen precursor ($Sb_2O_3$ or $BiBr_3$, respectively) in concentrated HBr. According to the composition of the final product, the hydroxyl ligand $OH^-$ of initial ruthenium complex is substituted during the reaction by the $Br^-$. This behavior is well known for the ruthenium hydroxyl complexes [19,21,26]. The precursor *trans*-$[RuNOPy_4F](ClO_4)_2$ was tested as well for the preparation of **2**. The fluoride ligand $F^-$ also can be substituted by the $Br^-$ in ruthenium complex leading to the precipitation of the same product $(H_3O)[RuNOPy_4Br]_4[Bi_2Br_9]_3{\cdot}3H_2O$, as confirmed by PXRD. Both compounds are stable at room temperature in ambient conditions and do not require any specifics for storage.

The structure of $[RuNOPy_4Br]_4[Sb_2Br_8][Sb_3Br_{12}]_2$ (**1**) belongs to monoclinic crystal system, space group $P2_1/c$, the unit cell parameters a = 12.022 Å, b = 22.454 Å, c = 26.372 Å, which results in a big unit cell volume (7112.2 $Å^3$), and asymmetric unit containing several different molecular ions. The presence of two chemically equivalent, but structurally different *trans*-$[RuNOPy_4Br]^{2+}$ cations might result in a different photochemical behavior of each photoswitchable molecule [27,28]. The asymmetric unit of **1** comprises the octahedrons *trans*-$[RuNOPy_4Br]^{2+}$, pyramidal dimers $[Sb_2Br_8]^{2-}$ and trinuclear anions $[Sb_3Br_{12}]^{3-}$. The asymmetric unit of the structure of **1** is shown in Fig. 1. According to the Cambridge Crystallographic Data Centre (CCDC) there is only one structure containing the $[Sb_3Br_{12}]^{3-}$ unit, $(Et(n\text{-}Pr)_3N)_3[Sb_3Br_{12}]$ [29]. The binuclear pyramidal anion $[Sb_2Br_8]^{2-}$ is more common, there are 6 hits in the CCDD [30–33]. The chosen intramolecular bond lengths are listed in Table 1. The average bond length $Sb\text{-}Br_{terminal}$ of $[Sb_2Br_8]^{2-}$ anion is slightly longer compared to that in $[Sb_3Br_{12}]^{3-}$ (2.69 vs. 2.59 Å), whereas the average bond length $Sb\text{-}Br_{bridge}$ is shorter (2.87 vs. 3.12 Å). Similar trend was found in bismuth clusters [34]. In the $[Sb_2Br_8]^{2-}$ the intramolecular contact Sb···Sb is 4.36 Å, which is longer than the sum of van der Waals Radii ($r_w$Sb=2.06 Å) [35]. The trinuclear anion $[Sb_3Br_{12}]^{3-}$ is distorted, the intramolecular distances Sb···Sb are 4.02, 4.18 and 4.68 Å, thus one short contact Sb···Sb (4.02 Å) is within the sum of $r_w$ [29]. Two crystallographically non-equivalent ruthenium cations *trans*-$[RuNOPy_4Br]^{2+}$ are present in the structure of **1**. The average bond lengths of the Ru-NO, N-O, Ru-Br and $Ru\text{-}N_{Py}$ groups are 1.78, 1.10, 2.47 and 2.11 Å, respectively, which are similar to those reported for *trans*-$[RuNOPy_4Br](PF_6)_2$ [20].

The intermolecular contacts are mostly represented by the hydrogen bonds Br···H-C with average distance Br···C of 3.63 Å, that are formed by the bromine atoms of $[Sb_2Br_8]^{2-}$ and $[Sb_3Br_{12}]^{3-}$ anions with the hydrogen atoms of pyridine ligands of the ruthenium cation. The nitrosyl ligands NO also form several contacts Br···O with average distance of 3.31 Å.

In order to get a better insight into the intermolecular contacts distribution, the two-dimensional fingerprints of Hirshfeld surfaces of *trans*-$[RuNOPy_4Br]^{2+}$ were plotted (see Fig. 2).

The biggest contribution to the whole Hirshfeld surface is made by hydrogen atoms of pyridine ligands, representing 75% of the surface (panels *a* and *b* of Fig. 2). From these contacts the strongest and the most frequent intermolecular interactions are represented by the H···Br, which occupy 42% of the surface. The second biggest contribution to the whole Hirshfeld surface is constituted by the weak H···H contacts holding 25% of the surface. On the level of structural packing, the ruthenium cations and Sb clusters form chains connected by means of weak Br···H-C contacts.

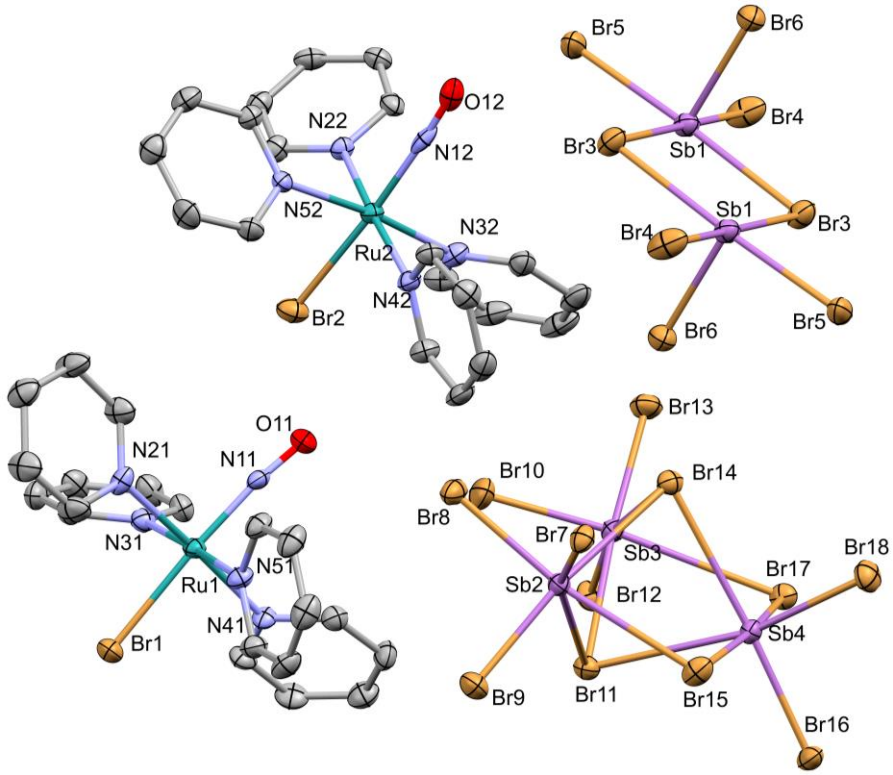


**Fig. 1.** The asymmetric unit of the structure of $[RuNOPy_4Br]_4[Sb_2Br_8][Sb_3Br_{12}]_2$ (**1**). Hydrogen atoms are omitted for clarity.

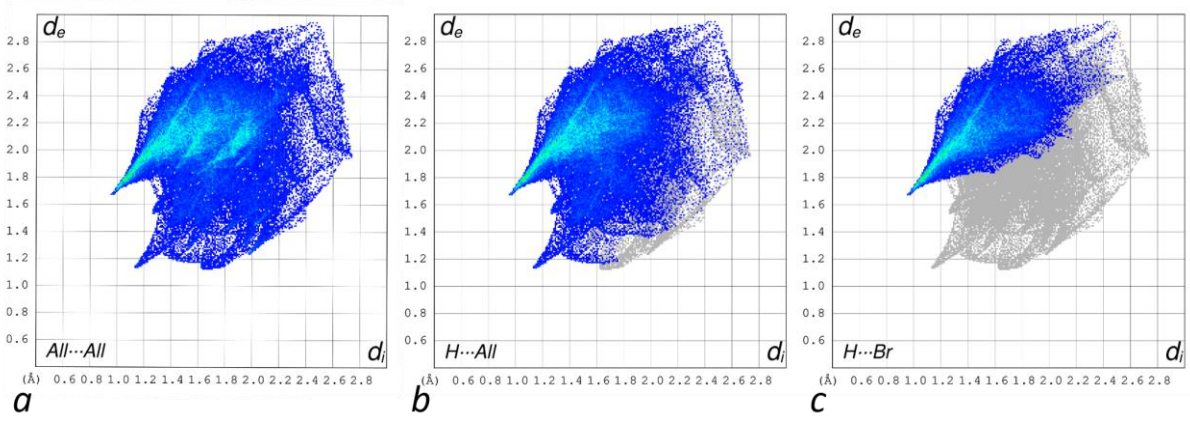


**Fig. 2.** The two-dimensional fingerprints of Hirshfeld surface of the *trans*-$[RuNOPy_4Br]^{2+}$ in **1** for the All···All, (a), H···All (b) and H···Br (c) contacts.

**Table 1.** Selected bond lengths Å in **1**. In *trans*-$[RuNOPy_4Br]^{2+}$ the parameters related to the crystallographically different units are separated by "/".

| *trans*-$[RuNOPy_4Br]^{2+}$ | | $[Sb_2Br_8]^{2-}$ | | $[Sb_3Br_{12}]^{3-}$ | |
|---|---|---|---|---|---|
| Ru-NO | 1.765(3)/ 1.797(3) | Sb-Br | 2.511(2); 2.691(1); 2.581(1) | Sb-Br | 2.621(1); 2.571(1); 2.562(1); 2.601(1); 2.624(1); 2.540(1); 2.569(1); 2.610(1) |
| N-O | 1.139(4)/ 1.052(5) | Sb-μ-Br | 2.868(1) | Sb-μ-Br | 3.253(1); 3.129(1); 3.027(1); 3.327(1); 3.251(1); 3.176(1); 2.729(1); 2.831(1); 3.407(1); 3.089(1) |
| Ru-Br | 2.472(1)/ 2.466(1) | - | - | - | - |
| $Ru-N_{Py}$ | 2.122(4); 2.100(3); 2.106(3); 2.105(3)/ 2.112(3); 2.110(4); 2.102(3); 2.105(3) | - | - | - | - |

The structure of $(H_3O)[RuNOPy_4Br]_4[Bi_2Br_9]_3{\cdot}3H_2O$ (**2**) possess lower symmetry (triclinic, P-1), and also quite big unit cell volume (6790.4 Å, see Table S1), providing even greater number of structurally different molecules (see asymmetric unit in Fig. S3). The fragment of the structure of **2** is shown in Fig. 3. The structure comprises four structurally non-equivalent *trans*-$[RuNOPy_4Br]^{2+}$ cations with slightly different intramolecular bond lengths (see Table 2), three non-equivalent $[Bi_2Br_9]^{3-}$ anions [36–38], three solvate water molecules and one $H_3O^+$. In the $[Bi_2Br_9]^{3-}$ anions the average bond length $Bi\text{-}Br_{terminal}$ is 2.76 Å, which is shorter with respect to $Bi\text{-}Br_{bridge}$ distance (3.02 Å), similar to **1**. In average, the intramolecular contacts Bi···Bi are 4.03 Å, which is shorter than the sum of $r_w$ of Bi atoms (2.54 Å) [35] and common for these compounds [39]. The average bond distances within the *trans*-$[RuNOPy_4Br]^{2+}$ cation are also similar to those in **1** and reach 1.77, 1.11, 2.46 and 2.11 Å for Ru-NO, N-O, Ru-Br and $Ru\text{-}N_{Py}$, respectively.

Similar to the previous structure, bromine atoms of $[Bi_2Br_9]^{3-}$ anions form intermolecular contacts Br···H-C, the average length of the Br···C distance is 3.65 Å. Additionally, there are contacts Br···H-O between $[Bi_2Br_9]^{3-}$ and water molecules with average Br···O distance of 3.31 Å. The nitrosyl ligands form several types of contacts O···X with bromine atoms of $[Bi_2Br_9]^{3-}$ anions, hydrogen atoms of pyridine rings and hydrogen atoms of solvate water molecules with average distances 3.21, 3.32 and 3.27 Å, respectively.

According to the 2D fingerprints of the Hirshfeld surface of *trans*-$[RuNOPy_4Br]^{2+}$ in **2** (see Fig. 4), the biggest contribution to the entire surface is made by the intermolecular contacts of hydrogen atoms of pyridine ligands (75%). Analogous to **1**, the large part of those contacts is represented by the H···Br interactions (34%), the majority of these contacts are relatively strong, which can be observed as a bright blue spike in Fig. 4. The rest of the contacts are mainly represented by the H···H interactions (33%). Similar to crystal packing of **1**, the $[Bi_2Br_9]^{3-}$ anions and ruthenium cations form chains organized by the Br···H-C and Br···H-O interactions.

Comparing the structures of **1** and **2**, the change of the pnictogen leads to a drastic change of the structural type of the pnictogen cluster. In **1** the structure comprises two types of clusters

with different nuclearity ($[Sb_2Br_8]^{2-}$ and $[Sb_3Br_{12}]^{3-}$), whilst in **2** only one but different type of the anion is formed ($[Bi_2Br_9]^{3-}$). The average bond lengths in *trans*-$[RuNOPy_4Br]^{2+}$ cation remains similar for both compounds. Based on the Hirshfeld surfaces analysis, in both **1** and **2** the intermolecular interactions are mainly represented by the Br···H-C contacts, reaching about 40% of the whole Hirshfeld surfaces. By means of these contacts (and also Br···H-O in **2**) the structures are packed as the chains of ruthenium cations and pnictogen clusters.

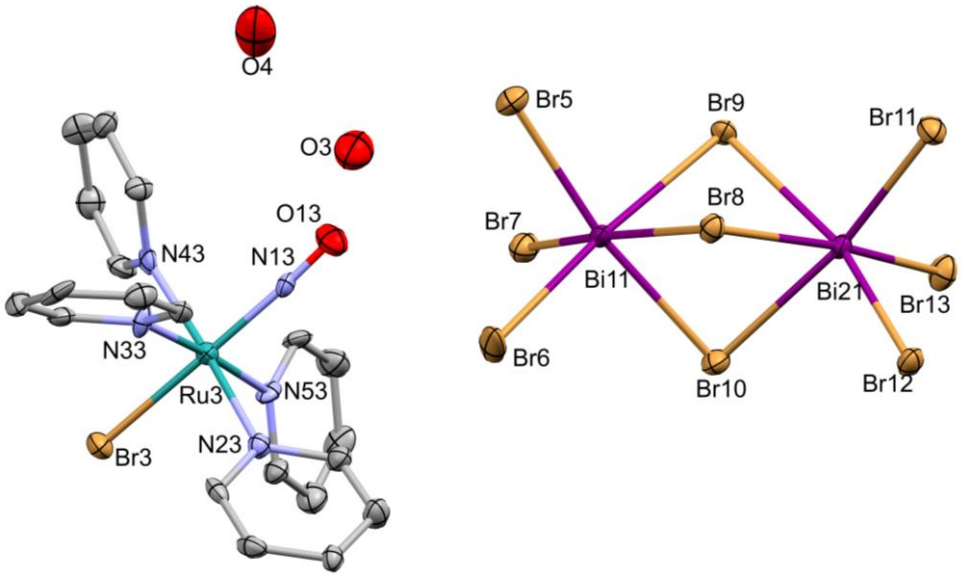


**Fig. 3.** The fragment of the structure of $(H_3O)[RuNOPy_4Br]_4[Bi_2Br_9]_3{\cdot}3H_2O$ (**2**). Hydrogens atoms are omitted for clarity.

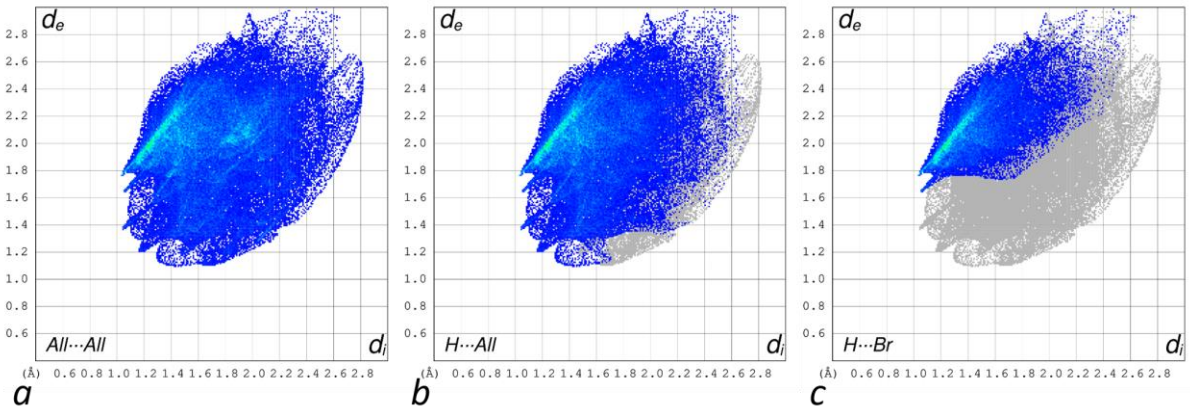


**Fig. 4.** The two-dimensional fingerprints of Hirshfeld surface of the *trans*-$[RuNOPy_4Br]^{2+}$ in **2** for the All···All, (a), H···All (b) and H···Br (c) contacts.

**Table 2.** Selected bond lengths Å in **2**. In *trans*-$[RuNOPy_4Br]^{2+}$ the parameters related to the crystallographically different units are separated by "/".

| *trans*-$[RuNOPy_4Br]^{2+}$ | $[Bi_2Br_9]^{3-}$ |
|---|---|

| | | | |
|---|---|---|---|
| Ru-NO | 1.755(8)/ 1.760(8)/ 1.789(7)/ 1.78(1) | Bi-Br | 2.689(1); 2.727(1); 2.742(2); 2.822(1); 2.707(2); 2.773(1); 2.738(2); 2.635(2); 2.84(1); 2.977(1); 2.700(2); 2.700(2); 2.735(1); 2.694(2); 2.709(2); 2.840(1); 2.734(2); 2.84(1) |
| N-O | 1.14(1)/ 1.12(1)/ 1.09(1)/ 1.09(2) | Bi-μ-Br | 3.018(2); 2.986(1); 2.928(2); 3.072(1); 3.058(2); 3.076(2); 2.920(1); 3.117(1); 3.051(1); 2.943(1); 3.048(1); 2.997(1); 3.087(1); 2.964(1); 3.180(2); 2.794(1); 3.081(2); 3.018(2) |
| Ru-Br | 2.448(1)/ 2.456(1)/ 2.463(1)/ 2.461(1) | - | - |
| $Ru-N_{Py}$ | 2.12(1); 2.10(1); 2.12(1); 2.13(1)/ 2.12(1); 2.10(1); 2.11(1); 2.14(1)/ 2.10(1); 2.10(1); 2.11(1); 2.14(1)/ 2.09(1); 2.11(1); 2.11(1); 2.11(1) | - | - |

**Photogeneration of linkage isomers**

The photoinduced linkage isomers in **1** and **2** were investigated by using IR-spectroscopy in the temperature range of 100-300 K. In the spectrum of **1** at 100 K the band of ν(NO) vibration has a maximum at 1890 $cm^{-1}$. Further intense bands are assigned to the pyridine vibrations at 1610, 1451, 1298, 1067, 1017, 752 and 689 $cm^{-1}$ (see Fig. S4). The irradiation of the sample at 100 K by the 365 nm light induces the appearance of the band at 1738 $cm^{-1}$ and a corresponding decrease of the ν(NO) band of GS (see Fig. 5, *a*). The maximum at 1738 $cm^{-1}$ is assigned to the ν(NO) band of the MS1 linkage isomer (Ru-ON), based on the corresponding observations in the earlier reported related compounds [19,20]. Different photoexcitation wavelengths (405, 420, 455, 470 nm) were tested for the photogeneration of MS1, however, the highest population of MS1 was observed in case of 365 nm. The population of MS1 was calculated from the decrease of the ν(NO) band of GS using the equation $P=100-(I(\nu(NO))_{GS\ after}/\ I(\nu(NO))_{GS\ before})\cdot 100$, which reaches 2% in case of **1**. The irradiation of MS1 with 660 or 1050 nm light induced the transfer of MS1 back to GS.

The thermal stability of MS1 was estimated by the gradual heating of the sample, as a result, an efficient thermal decay of MS1 to GS occurs at T >200 K. Since the MS1 band is broadened significantly at higher temperatures, it was not possible to precisely determine the kinetic parameters of the MS1→GS decay process.

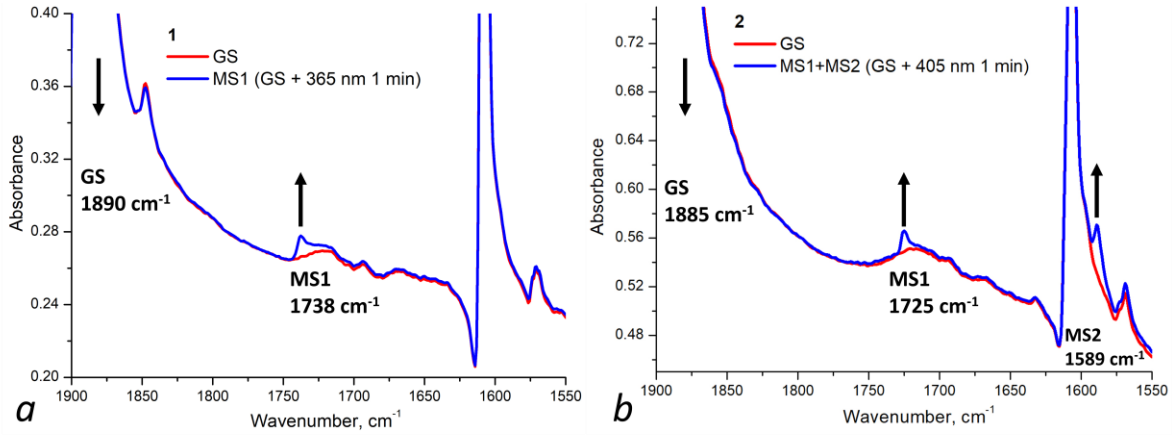


**Fig. 5.** IR-spectra of **1** (panel *a*) and **2** (panel *b*) before (GS) and after irradiation with 365 or 405 nm (MS1) measured at 100 K.

The IR-spectrum of **2** is similar to that of **1** (see Fig. S5). The ν(NO) band in GS at 100 K is at 1885 $cm^{-1}$ with a shoulder at 1899 $cm^{-1}$, the most intense pyridine bands are observed at 1610, 1451, 1298, 1067, 1017, 752 and 689 $cm^{-1}$. Interestingly, the irradiation of the sample by 365 or 405 nm light induces the formation of two isomers - MS1 and MS2 (Ru-$\eta^2$-(NO)) with ν(NO) bands at 1725 and 1589 $cm^{-1}$, respectively (see Fig. 5, *b*), whereby irradiation with 405 nm generates a slightly bigger amount of MS2, and 365 nm more of MS1. The total population is 3%. Additionally, a band with maximum at 572 $cm^{-1}$ appears, which is tentatively assigned to the ν(Ru-NO)/δ(Ru-N-O) vibration of MS2. The corresponding low intense band of GS is found at 592 $cm^{-1}$. It is important to mention that irradiation at 455 nm decreases the population of both metastable states, and the excitation at 650 (660) or 980 (1050) nm completely transfer both MS1 and MS2 back to GS.

The thermal stability of MS1 and MS2 was measured by IR-spectroscopy in isothermal mode. Once the rate constants of the MS1/MS2→GS reactions were measured at certain temperatures, the activation energy ($E_a$) and frequency factor ($lgk_0$) were determined from the Arrhenius plot (see Fig. 6). The parameter $T_d$ (decay temperature) was calculated using Arrhenius equation from the obtained $E_a$ and $lgk_0$ at $k=10^{-3}$ $s^{-1}$ [40]. This parameter is very useful for the comparison of thermal stability of different compounds. The kinetic parameters are gathered in Table 3. Thus, MS1 efficiently decays to GS at temperatures higher than 200 K, similar to **1**. Roughly, the lifetime of MS1 at $T_d$, which equals to 199 K, is around 17 min. Thermal stability of MS2 is lower than that of MS1, with a $T_d$ of 139 K (see Table 3). Commonly, MS2 has lower thermal stability than MS1, as described for the related compounds [19]. Comparing thermal stability of **2** with that of related complex *trans*-[RuNOPy$_4$Br](PF$_6$)$_2$, for which $T_d$ of MS1 and MS2 are 201 and 131 K, respectively, a small thermal stabilization of MS2 in **2** is observed. Indeed, the change of the counterion can lead to the change of the thermal stability of the linkage isomer [41,42].

Another interesting feature of the linkage isomers in **1** and **2**, is that the highest population of metastable states is observed after 365 nm irradiation in both compounds. For example, in the related complex *trans*-[RuNOPy$_4$Br](PF$_6$)$_2$ the population of MS1 reaches about 40% after 505 nm irradiation and gets lower in case of 365 nm excitation [19,20]. Thus, there are significant differences in population and wavelength for the efficient generation of MS1/MS2 ($\lambda_{top}$). Earlier it was

reported that shorter intermolecular contacts between the NO ligand and the atoms of the second coordination sphere lead to a higher population of MS1 [20]. Indeed, in *trans*-[RuNOPy$_4$Br](PF$_6$)$_2$ the shortest contacts between NO and $PF_6^-$ anions are 2.680, 2.696 Å, which are shorter compared to intermolecular contacts NO···X in **1** and **2** (about 3.3 Å). Apparently, the large difference in $\lambda_{top}$ (505 vs. 365 nm) is related to the difference in absorption spectra of all linkage isomers GS, MS1 and MS2 [16,41]. Assuming that the mechanism of NO isomerization is the two-step process GS→MS2→MS1, the absorption cross section at excitation wavelength of each isomer plays a crucial role [43–45]. Earlier it was shown that counterion can sufficiently change the absorption spectrum of any isomer [41]. In case of **1** and **2** we assume that the spectra of MS1 and MS2 are significantly different from those reported for *trans*-[RuNOPy$_4$Br](PF$_6$)$_2$ [19]. Unfortunately, the low population of metastable states prevents the detection of MS1/MS2 signatures using UV-vis spectroscopy (GS spectra of **1** and **2** are shown in Fig. S6). Generally, to reach a high population of MS1, a high absorption of both GS and MS2 and a low absorption of MS1 at certain excitation wavelength is necessary [16]. For example, in related complex *trans*-[RuNOPy$_4$Cl](PF$_6$)$_2$ the maximum population of MS1 (76%) was found after excitation at 476.5 nm, where the absorption coefficient of MS1 is minimal [46]. Similar situation was found in *trans*-[RuNOPy$_4$Br](PF$_6$), where the absorption minimum of MS1 was observed at 490 nm, giving the best population (40%) after 505 nm exposure [19]. Such photochemical behavior is related to the two-step mechanism of MS1 formation (GS→MS2→MS1) [43–45]. According to the mechanism, the first photon absorbed by GS drives system to MS2 configuration, following absorption of the photon by MS2 may excite the system to MS1. Importantly, the efficiency of light excitation of each state is determined by the efficiency of cross-section or absorption coefficient at given wavelength. Also, higher absorption coefficient of MS1 at certain wavelength results in higher probability of backward reactions MS1→GS/MS2. Thus, the population of certain isomer is governed by the photochemical equilibrium during GS↔MS2↔MS1 transformations, where lower MS1 deexcitation probability results in its higher population. Based on this, we assume that relative minimum of MS1 absorption band lies in the range of 365 nm. Another possible reason of the low population of metastable states might be hidden in properties of halometalate anions. According to the literature data, bismuth and antimony compounds might exhibit light emission in green-red range after UV-exposure [47–51]. Since light irradiation by the red light (650-660 nm) of MS1,2 leads to the depopulation of both states back to GS, possible emission by the halometalate in the red range might decrease the population of both states. Though the embedding of a photoswitchable compound into a matrix might results in higher photoconversion fraction [52,53], the light absorption by the bismuth or antimony complex also might decrease the probability of excitation of nitrosyl compound [41,54].

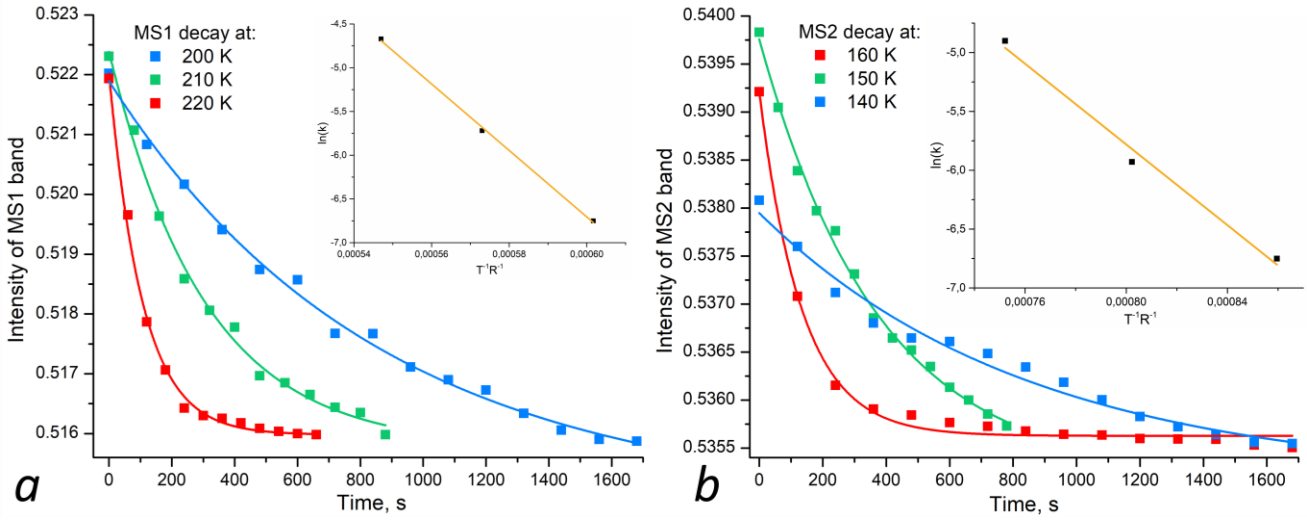


**Fig. 6.** The thermal decay of the ν(NO) band of MS1 (panel *a*) and MS2 (panel **b**) in **2** at different temperatures. Corresponding Arrhenius plots are shown in the inserts.

**Table 3.** The kinetic parameters of MS1⟶GS and MS2⟶GS transformations in **2**: rate constant (k), activation energy ($E_a$), frequency factor ($lgk_0$) and decay temperature ($T_d$).

| MS1 | | | MS2 | | |
|---|---|---|---|---|---|
| $E_a$, kJ mol$^{-1}$ | $lgk_0$ | $T_d$, K | $E_a$, kJ mol$^{-1}$ | $lgk_0$ | $T_d$, K |
| 38.00 ±1.24 | 7.00±0.31 | 199 | 17.15 ±1.77 | 3.45±0.62 | 139 |
| k·10$^{-3}$, s$^{-1}$ | | | k·10$^{-3}$, s$^{-1}$ | | |
| $k_{220}$ | 9.37±0.41 | | $k_{160}$ | 7.44±0.35 | |
| $k_{210}$ | 3.28±0.24 | | $k_{150}$ | 2.66±0.19 | |
| $k_{200}$ | 1.17±0.09 | | $k_{140}$ | 1.17±0.19 | |

## Conclusions

Using a simple synthetic approach the compounds $[RuNOPy_4Br]_4[Sb_2Br_8][Sb_3Br_{12}]_2$ (**1**) and $(H_3O)[RuNOPy_4Br]_4[Bi_2Br_9]_3{\cdot}3H_2O$ (**2**) were obtained mixing the ruthenium nitrosyl species and corresponding $Sb_2O_3$ or $BiBr_3$ precursor in HBr. The XRD analysis of the structures of **1** and **2** shows that the type of pnictogen affects the structural type by forming binuclear bismuth and bi- and tri-nuclear antimony halide anions. The Hirshfeld surfaces analysis reveals for both **1** and **2** that the intermolecular interactions are mainly represented by Br···H-C contacts, reaching about 40% of the whole Hirshfeld surfaces. The light irradiation of **1** and **2** at 365 or 405 nm leads to the isomerization of the Ru-NO (GS) group of the ruthenium cation *trans*-$[RuNOPy_4Br]^{2+}$ to the metastable isomer Ru-ON (MS1). In **2** the side-bond isomer Ru-$\eta^2$-(NO) (MS2) can be photoinduced as well. Based on the IR-spectroscopy data the total population of linkage isomers

in both compounds does not exceed 3%. Importantly, the backward reaction MS1/MS2→GS can be induced by red-infrared light. The thermal stability of both metastable states was investigated by IR-spectroscopy in isothermal mode. It was found that MS1 decays efficiently at T>200 K and MS2 is less stable decaying at T>140 K. For the compound **2** the activation energies ($E_a$) and frequency factors ($lgk_0$) of the MS1→GS and MS2→GS reactions were determined amounting to 38.00 ±1.24 kJ $mol^{-1}$, 7.00±0.31 and 17.15 ±1.77 kJ $mol^{-1}$, 3.45±0.62, respectively. The obtained results were compared with corresponding photochemical properties of the related *trans*-$[RuNOPy_4Br](PF_6)_2$ complex. It was shown that the ruthenium complex combined with pnictogen cluster demonstrates quite different behavior, namely the population of the metastable states drops down significantly (from 40 to 3%), and the wavelength for efficient metastable states generation shifts to the UV range (from 505 to 365 nm). We assume that both differences are related to the difference in absorption spectra of all linkage isomers GS, MS1 and MS2 in **1** and **2**. In **2** the advantage of the $[Bi_2Br_9]^{3-}$ cluster introduction is the increase of MS2 isomer decay temperature ($T_d$) with respect to that in *trans*-$[RuNOPy_4Br](PF_6)_2$ by about 10 K (139 vs. 131 K). Thus, the properties of light induced linkage isomers can be drastically changed by the introduction of the pnictogen cluster. Based on the obtained results we can expect that other photoswitchable compounds (containing $NO_2$ or $SO_2$-like ligands) [55,56] can be embedded into pnictogen halide structures, that will provide further opportunities for the design of Bi and Sb clusters coupled to photosensitive complexes.

**Acknowledgements**

The work has been supported by grant of Russian Science Foundation (22-43-09001, https://rscf.ru/project/22-43-09001/) and ANR (grant no. ANR-21-CE30-0045-01) in the part of synthesis of ruthenium compounds and spectroscopic experiments. The research was supported by the Ministry of Science and Higher Education of the Russian Federation, N 121031700315-2 in the part of physical chemical characterization of ruthenium complexes. Artem Mikhailov is grateful for financial support from the Metchnikov bourse program 2021. Authors thank Piryazev D.A. for the measurement of X-ray diffraction of **2** single crystal on XRD Facility of NIIC SB RAS.

**References**

1 I. C. Smith, E. T. Hoke, D. Solis-Ibarra, M. D. McGehee and H. I. Karunadasa, *Angew. Chemie Int. Ed.*, 2014, **53**, 11232–11235.

2 P. Müller-Buschbaum, M. Thelakkat, T. F. Fässler and M. Stutzmann, *Adv. Energy Mater.*, 2017, **7**, 1700248.

3 I. Gelmetti, N. F. Montcada, A. Pérez-Rodríguez, E. Barrena, C. Ocal, I. García-Benito, A. Molina-Ontoria, N. Martín, A. Vidal-Ferran and E. Palomares, *Energy Environ. Sci.*, 2019, **12**, 1309–1316.

4 J. K. Pious, C. Muthu, S. Dani, A. Saeki and C. Vijayakumar, *Chem. Mater.*, 2020, **32**, 2647–2652.

5 Y. Yang, C. Liu, M. Cai, Y. Liao, Y. Ding, S. Ma, X. Liu, M. Guli, S. Dai and M. K. Nazeeruddin, *ACS Appl. Mater. Interfaces*, 2020, **12**, 17062–17069.

6 S. A. Adonin, L. A. Frolova, M. N. Sokolov, G. V. Shilov, D. V. Korchagin, V. P. Fedin, S. M. Aldoshin, K. J. Stevenson and P. A. Troshin, *Adv. Energy Mater.*, 2018, **8**, 1701140.

7 L. Zhang, K. Wang and B. Zou, *ChemSusChem*, 2019, **12**, 1612–1630.

8 Z. Jin, Z. Zhang, J. Xiu, H. Song, T. Gatti and Z. He, *J. Mater. Chem. A*, 2020, **8**, 16166–16188.

9 Q. Jiang, Y. Zhao, X. Zhang, X. Yang, Y. Chen, Z. Chu, Q. Ye, X. Li, Z. Yin and J. You, *Nat. Photonics*, 2019, **13**, 460–466.

10 C. Li, J. Yin, R. Chen, X. Lv, X. Feng, Y. Wu and J. Cao, *J. Am. Chem. Soc.*, 2019, **141**, 6345–6351.

11 Z. Fang, L. Wang, X. Mu, B. Chen, Q. Xiong, W. D. Wang, J. Ding, P. Gao, Y. Wu and J. Cao, *J. Am. Chem. Soc.*, 2021, **143**, 18989–18996.

12 M. Alidaei, V. Ahmadi, S. M. Mousavi and F. A. Roghabadi, *J. Alloys Compd.*, 2022, **903**, 163891.

13 N. Fillafer, T. Seewald, L. Schmidt-Mende and S. Polarz, *Beilstein J. Nanotechnol.*, 2020, **11**, 466–479.

14 D. Schaniel, M. Imlau, T. Weisemoeller, T. Woike, K. W. Krämer and H.-U. Güdel, *Adv. Mater.*, 2007, **19**, 723–726.

15 P. Coppens, I. Novozhilova and A. Kovalevsky, *Chem. Rev.*, 2002, **102**, 861–884.

16 D. Schaniel and T. Woike, *Phys. Chem. Chem. Phys.*, 2009, **11**, 4298–4359.

17 A. A. Mikhailov, E. Wenger, G. A. Kostin and D. Schaniel, *Chem. – A Eur. J.*, 2019, **25**, 7569–7574.

18 D. Schaniel, B. Cormary, I. Malfant, L. Valade, T. Woike, B. Delley, K. W. Krämer and H. U. Güdel, *Phys. Chem. Chem. Phys.*, 2007, **9**, 3717–3724.

19 A. A. Mikhailov, G. A. Kostin and D. Schaniel, *New J. Chem.*, 2022, **46**, 12641–12650.

20 B. Cormary, S. Ladeira, K. Jacob, P. G. Lacroix, T. Woike, D. Schaniel and I. Malfant, *Inorg. Chem.*, 2012, **51**, 7492–7501.

21 G. A. Kostin, A. A. Mikhailov, N. V Kuratieva, D. P. Pishchur and A. N. Makhinya, *New J. Chem.*, 2018, **42**, 18928–18934.

22 G. M. Sheldrick, *Acta Crystallogr. Sect. A Found. Adv.*, 2015, **71**, 3–8.

23 O. V. Dolomanov, L. J. Bourhis, R. J. Gildea, J. A. K. Howard and H. Puschmann, *J. Appl. Crystallogr.*, 2009, **42**, 339–341.

24 F. L. Hirshfeld, *Theor. Chim. Acta*, 1977, **44**, 129–138.

25 M. A. Spackman and D. Jayatilaka, *CrystEngComm*, 2009, **11**, 19–32.

26 V. Vorobyev, A. A. Mikhailov, V. Y. Komarov, A. N. Makhinya and G. A. Kostin, *New J.*

*Chem.*, 2020, **44**, 4762–4771.

27 B. Cormary, I. Malfant, M. Buron-Le Cointe, L. Toupet, B. Delley, D. Schaniel, N. Mockus, T. Woike, K. Fejfarová, V. Petříček and M. Dušek, *Acta Crystallogr. Sect. B Struct. Sci.*, 2009, **65**, 612–623.

28 A. Gansmüller, A. A. Mikhailov, G. A. Kostin, J. Raya, C. Palin, T. Woike and D. Schaniel, *Anal. Chem.*, 2022, **94**, 4474–4483.

29 M. D. Petrov, M. N. Sokolov, V. P. Fedin and S. A. Adonin, *J. Struct. Chem.*, 2020, **61**, 1794–1799.

30 A. N. Usol'tsev, M. D. Petrov, I. V Korol'kov, M. N. Sokolov, V. A. Blatov and S. A. Adonin, *Russ. J. Coord. Chem.*, 2021, **47**, 620–625.

31 N. Leblanc, M. Allain, N. Mercier and E. Cariati, *Cryst. Growth Des.*, 2011, **11**, 5200–5205.

32 S. Pohl, W. Saak, R. Lotz and D. Haase, *Zeitschrift für Naturforsch. B*, 1990, **45**, 1355–1362.

33 M. Wojciechowska, P. Szklarz, A. Białońska, J. Baran, R. Janicki, W. Medycki, P. Durlak, A. Piecha-Bisiorek and R. Jakubas, *CrystEngComm*, 2016, **18**, 6184–6194.

34 S. A. Adonin, M. N. Sokolov and V. P. Fedin, *Coord. Chem. Rev.*, 2016, **312**, 1–21.

35 M. Mantina, A. C. Chamberlin, R. Valero, C. J. Cramer and D. G. Truhlar, *J. Phys. Chem. A*, 2009, **113**, 5806–5812.

36 W. Zhang, M. Hong and J. Luo, *J. Am. Chem. Soc.*, 2021, **143**, 16758–16767.

37 S. A. Adonin, I. D. Gorokh, A. S. Novikov, D. G. Samsonenko, I. V. Yushina, M. N. Sokolov and V. P. Fedin, *CrystEngComm*, 2018, **20**, 7766–7772.

38 V. Y. Kotov, A. B. Ilyukhin, P. A. Buikin, N. P. Simonenko, A. A. Korlyukov, A. F. Smol'yakov, K. E. Yorov and A. V. Gavrikov, *Dalt. Trans.*, 2019, **48**, 7602–7611.

39 P. R. Varadwaj, A. Varadwaj, H. M. Marques and K. Yamashita, , DOI:10.48550/arXiv.2209.07319.

40 Y. Morioka, A. Ishikawa, H. Tomizawa and E. Miki, *J. Chem. Soc. Dalt. Trans.*, 2000, **54**, 781–786.

41 A. A. Mikhailov, V. Y. Komarov, A. S. Sukhikh, D. P. Pishchur, D. Schaniel and G. A. Kostin, *New J. Chem.*, 2020, **44**, 18014–18024.

42 H. Zöllner, W. Krasser, T. Woike and S. Haussühl, *Chem. Phys. Lett.*, 1989, **161**, 497–501.

43 F. Talotta, J.-L. Heully, F. Alary, I. M. Dixon, L. González and M. Boggio-Pasqua, *J. Chem. Theory Comput.*, 2017, **13**, 6120–6130.

44 F. Talotta, M. Boggio-Pasqua and L. González, *Chem. – A Eur. J.*, 2020, **26**, 11522–11528.

45 F. Talotta, L. González and M. Boggio-Pasqua, *Molecules*, 2020, **25**, 2613.

46 D. Schaniel, B. Cormary, I. Malfant, L. Valade, T. Woike, B. Delley, K. W. Krämer and H. U. Güdel, *Phys. Chem. Chem. Phys.*, 2007, **9**, 3717–3724.

47 H. Wang, J. Tian, K. Jiang, Y. Zhang, H. Fan, J. Huang, L. Yang, B. Guan and Y. Song, *RSC Adv.*, 2017, **7**, 43826–43830.

48 L. Romagnoli, A. D'Annibale, E. Blundo, A. Polimeni, A. Cassetta, G. Chita, R. Panetta, A. Ciccioli and A. Latini, *Cryst. Growth Des.*, 2022, **22**, 7426–7433.

49 B. V. Bukvetskii, T. V. Sedakova and A. G. Mirochnik, *J. Struct. Chem.*, 2009, **50**, 322–327.

50 J. Kim, J. Park, S.-W. Nam, M. Shin, S. Jun, Y.-H. Cho and B. Shin, *ACS Appl. Energy Mater.*, 2020, **3**, 4650–4657.

51 S. Premkumar, D. Liu, Y. Zhang, D. Nataraj, S. Ramya, Z. Jin, B. B. Mamba, A. T. Kuvarega and J. Gui, *ACS Appl. Nano Mater.*, 2020, **3**, 9141–9150.

52 P. Coppens, S.-L. Zheng, M. Gembicky, M. Messerschmidt and P. M. Dominiak, *CrystEngComm*, 2006, **8**, 735.

53 V. Greussing, J. M. Gallmetzer, H. Huppertz, T. S. Hofer and H. A. Schwartz, *J. Phys. Chem. C*, 2022, **126**, 10923–10931.

54 L. E. Hatcher, J. M. Skelton, M. R. Warren and P. R. Raithby, *Acc. Chem. Res.*, 2019, **52**, 1079–1088.

55 A. A. Cordones, J. H. Lee, K. Hong, H. Cho, K. Garg, M. Boggio-Pasqua, J. J. Rack, N. Huse, R. W. Schoenlein and T. K. Kim, *Nat. Commun.*, , DOI:10.1038/s41467-018-04351-0.

56 L. E. Hatcher, M. R. Warren, D. R. Allan, S. K. Brayshaw, A. L. Johnson, S. Fuertes, S. Schiffers, A. J. Stevenson, S. J. Teat, C. H. Woodall and P. R. Raithby, *Angew. Chemie - Int. Ed.*, 2011, **50**, 8371–8374.

**Supplementary Information**

# Bismuth and antimony halometalates containing photoswitchable ruthenium nitrosyl complex

Artem Mikhailov[a], Nikita Korobeynikov[b], Andrey Usoltsev[b], Sergey A. Adonin[b], Gennadiy A. Kostin[b], Dominik Schaniel[a]

[a] Université de Lorraine, CNRS, CRM2, UMR 7036, Nancy 54000, France

[b] Nikolaev Institute of Inorganic Chemistry, Siberian Branch of the Russian Academy of Sciences, 3 Acad. Lavrentiev Avenue, Novosibirsk 630090, Russian Federation

**Table S1.** Experimental and refinement details.

| Complex | $[RuNOPy_4Br]_4[Sb_2Br_8][Sb_3Br_{12}]_2$ (**1**) | $(H_3O)[RuNOPy_4Br]_4[Bi_2Br_9]_3{\cdot}3H_2O$ (**2**) |
|---|---|---|
| Empirical formula | $C_{20}H_{20}Br_9N_5ORuSb_2$ | $C_{80}H_{89}Bi_6Br_{31}N_{20}O_8Ru_4$ |
| Formula weight | 1410.17 | 5593.07 |
| Temperature/K | 100 | 150 |
| Crystal system | monoclinic | triclinic |
| Space group | $P2_1/c$ | P-1 |
| a/Å | 12.0218(11) | 15.1913(13) |
| b/Å | 22.4544(19) | 17.2926(12) |
| c/Å | 26.372(2) | 27.970(3) |
| α/° | 90 | 96.349(3) |
| β/° | 92.506(3) | 103.183(3) |
| γ/° | 90 | 105.167(3) |
| Volume/Å$^3$ | 7112.2(11) | 6790.4(10) |
| Z | 8 | 2 |
| $\rho_{calc}$g/cm$^3$ | 2.634 | 2.735 |
| μ/mm$^{-1}$ | 12.064 | 17.348 |
| F(000) | 5152 | 5062 |
| Crystal size/mm$^3$ | 0.217 × 0.205 × 0.106 | 0.055 × 0.055 × 0.055 |
| Radiation | MoKα (λ = 0.71073) | MoKα (λ = 0.71073) |
| 2Θ range for data collection/° | 3.846 to 66.504 | 2.876 to 51.362 |
| Index ranges | -18 ≤ h ≤ 18, -34 ≤ k ≤ 34, -32 ≤ l ≤ 40 | -18 ≤ h ≤ 18, -21 ≤ k ≤ 21, -34 ≤ l ≤ 31 |
| Reflections collected | 256633 | 73912 |
| Independent reflections | 27174 [$R_{int}$ = 0.0953, $R_{sigma}$ = 0.0588] | 25709 [$R_{int}$ = 0.0590, $R_{sigma}$ = 0.0793] |
| Data/restraints/parameters | 27174/2/685 | 25709/12/1374 |
| Goodness-of-fit on $F^2$ | 1.053 | 1.044 |
| Final R indexes [I>=2σ (I)] | $R_1$ = 0.0393, $wR_2$ = 0.0780 | $R_1$ = 0.0525, $wR_2$ = 0.1066 |
| Final R indexes [all data] | $R_1$ = 0.0747, $wR_2$ = 0.0885 | $R_1$ = 0.0754, $wR_2$ = 0.1150 |
| Largest diff. peak/hole / e Å$^{-3}$ | 1.36/-1.82 | 3.25/-1.93 |

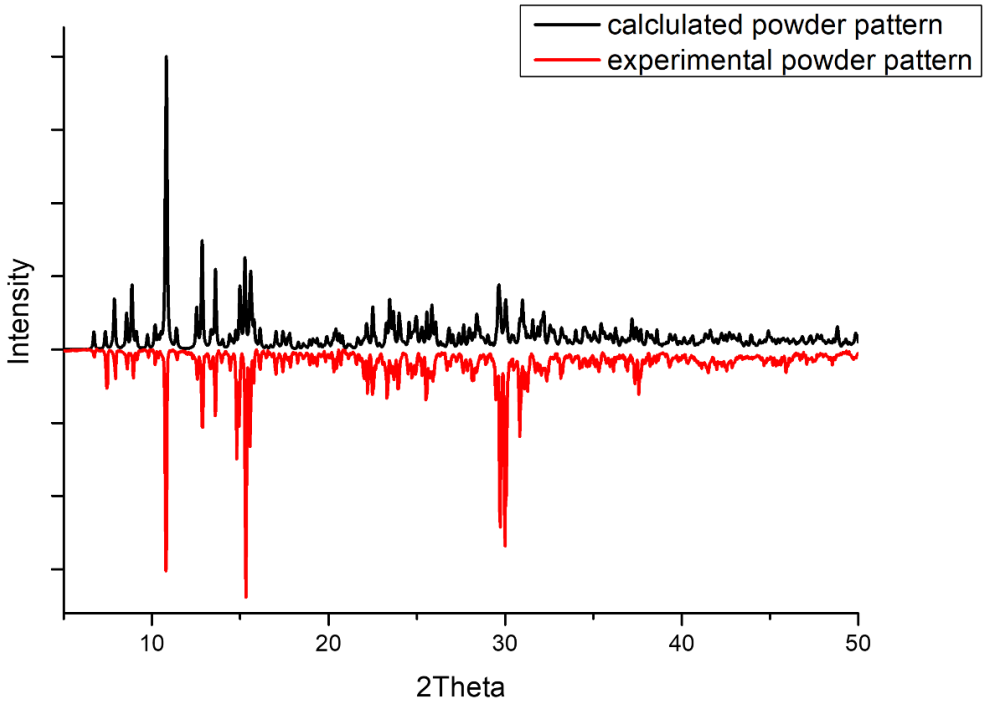


**Fig. S1**. PXRD data of **1**.

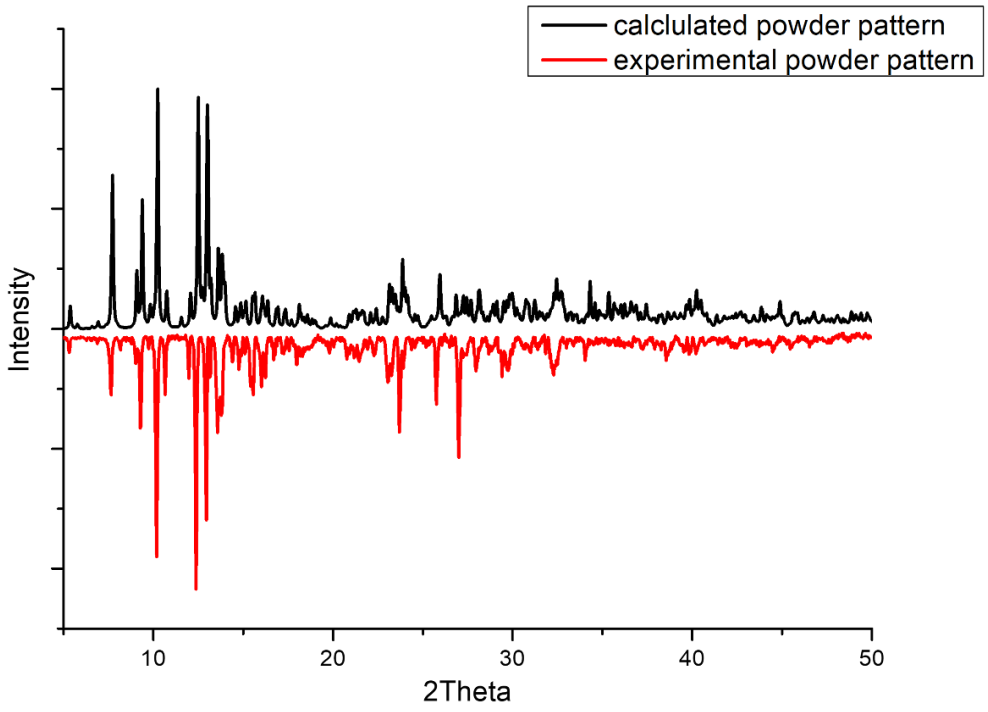


**Fig. S2**. PXRD data of **2**.

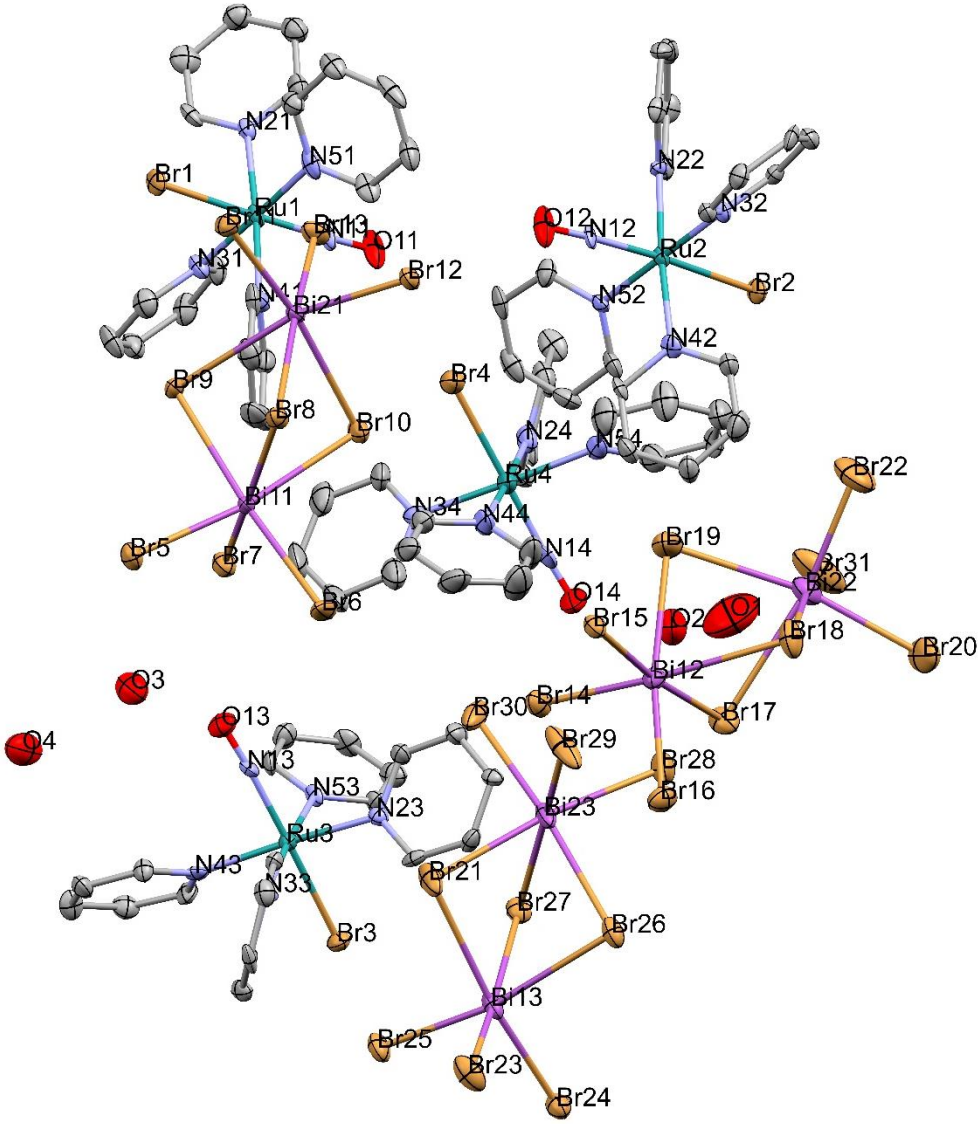


**Fig. S3.** The asymmetric unit of the structure of $(H_3O)[RuNOPy_4Br]_4[Bi_2Br_9]_3 \cdot 3H_2O$ (**2**). Hydrogen atoms are omitted for clarity.

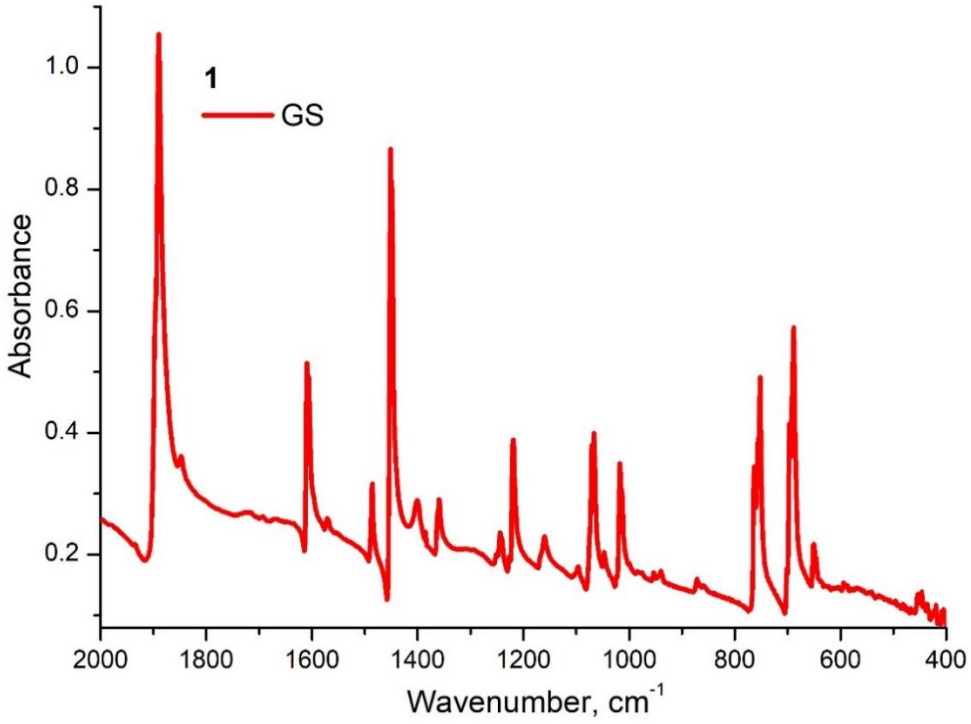


**Fig. S4**. IR-spectrum of **1** at 100 K.

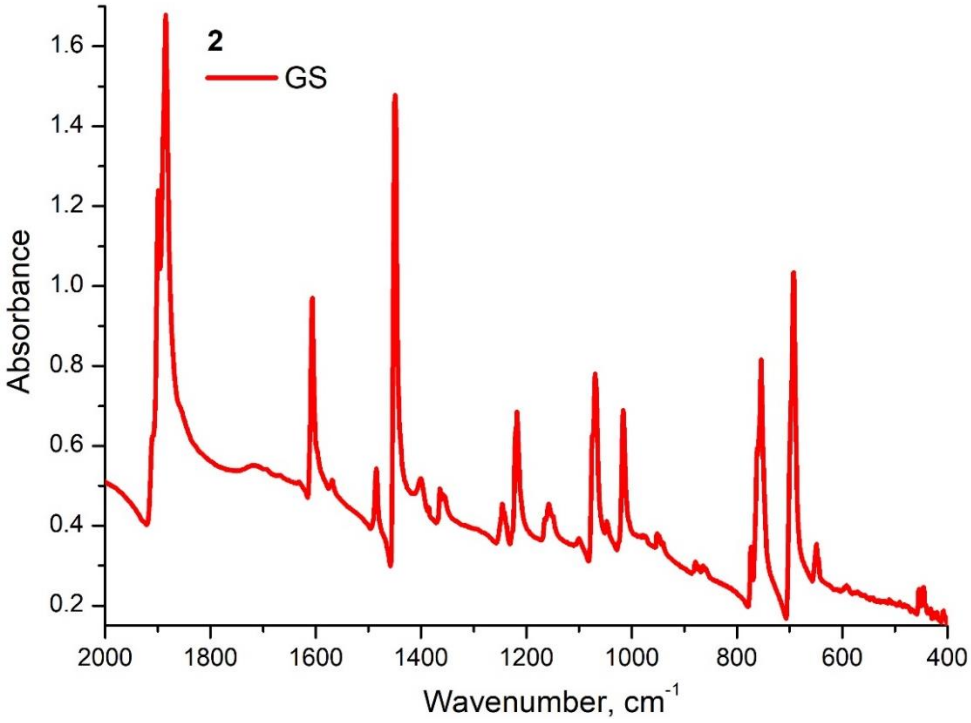


**Fig. S5**. IR-spectrum of **2** at 100 K.

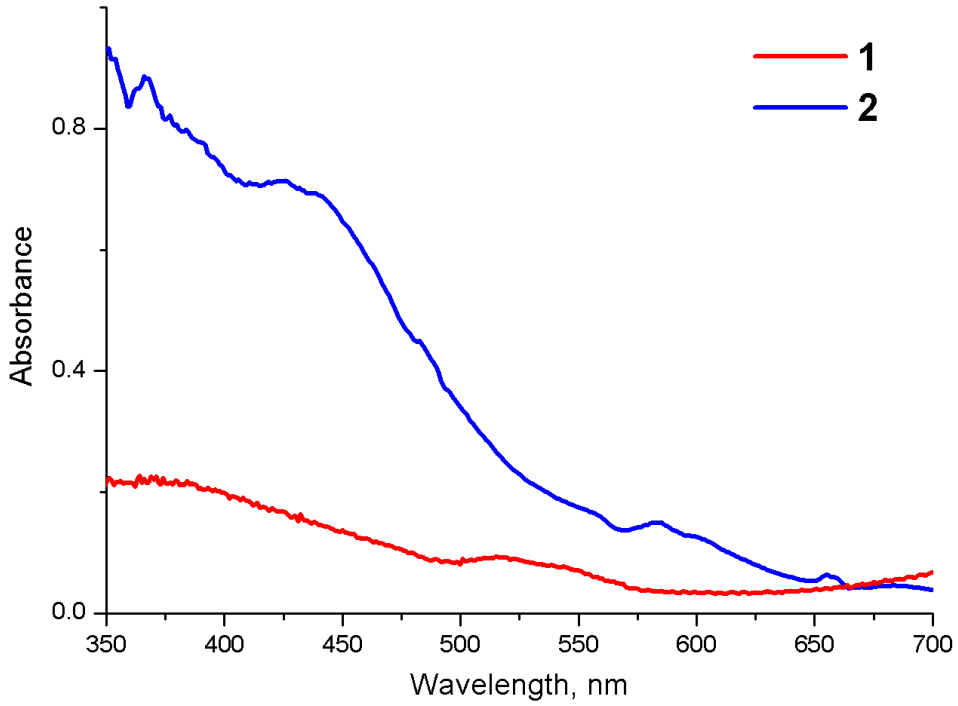


**Fig. S6**. UV-vis spectra of **1** and **2** in GS embedded into KBr matrix.